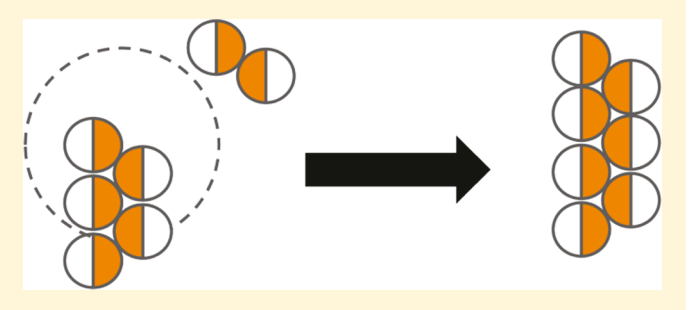
# Measuring, Modeling, and Predicting the Magnetic Assembly Rate of 2D-Staggered Janus Particle Chains

Thomas W. Long,<sup>†</sup> Ubaldo M. Córdova-Figueroa,<sup>‡</sup> and Ilona Kretzschmar\*,<sup>†</sup>

Supporting Information

ABSTRACT: The assembly of magnetic Janus particles in a quasi-two-dimensional environment with a dipole moment shifted from the center and oriented perpendicular to the Janus cap height is studied with optical microscopy and found to adhere to a general model accounting for the particle dipole strength, the particle Brownian dynamics, the initial concentration, and, most importantly, the magnetic dipole shift. The particle aggregates are treated as diffusing spherocylinders with length and width dependent on the magnetic dipole shift. Aggregation occurs irreversibly once



particle aggregates enter within a distance at which Brownian and dipole forces are equal, defined as the capture distance. The capture distance model is expressed as a general Smoluchowski coagulation rate kernel for chains of an arbitrary length, dipole strength, and dipole shift, allowing for aggregation rate predictions for related systems.

### ■ INTRODUCTION

When a uniform magnetic field is applied to a solution of dispersed magnetic colloids, the particles assemble into long linear chains parallel to the magnetic field. These chains resist shearing and raise the effective viscosity of the fluid as a monotonically increasing function of the field being applied. This property is employed in magnetorheological fluids (MRFs) that have numerous current industrial applications, such as magnetorheological dampers for vehicles,<sup>2</sup> and many potential applications, such as artificial flagella.<sup>3</sup> Current MRFs are limited by uncontrolled aggregation and the monotonic viscosity response, which might be addressed by a better understanding of the relationship among colloidal component, structure of aggregate, and rate of aggregation.<sup>2</sup>

Magnetic particle assembly rates have been studied to understand the nature of MRFs.4 Characterizing the rate of assembly is of academic and industrial interest as the transition from a colloidal dispersion to a shear resistant system of parallel chains influences the time-dependent material properties of the fluid.<sup>2</sup> The large parameter space (particle size, dipole strength, dipole position, concentration, viscosity, and temperature) requires a theoretical model to determine what kinds of particles will be most suited for a particular aggregation response. Such a theoretical model would likely consist of differential equations that can be numerically solved to yield predictions for aggregation rates of systems not yet synthesized.

Although much of the literature has focused on characterizing the kinetics of linear magnetic chains made up of

spherical particles with magnetic dipoles directly in their center, recent work has shown that the theoretical prediction of magnetic colloid assembly sometimes requires the use of a patchlike dipole rather than the standard point-dipole assumption due to minor anisotropies in the distribution of the magnetic components in the colloids. 5,6 Besides isotropic magnetic particles, other structures are also of interest.<sup>7</sup> One of those structures is the Janus particle. Janus particles are anisotropic particles with two halves of approximately equal size. 15 The two halves differ in at least one property, causing the interactions of the particles to be anisotropic as well. Since the first published example of controlled self-assembly of Janus particles, 16 it has been of interest to understand the impact of the building block asymmetry on the assembly rate. The thermodynamically stable structures that Janus particles selfassemble into have been widely studied and characterized. 17,18 However, general theories for the kinetics of the transition from individual particles to aggregates have been difficult to develop.19

Study of the synthesis of magnetic Janus particles has produced methods that reliably create Janus particles with desired qualities, 20,21 including shape, amphiphilicity, and other properties. For example, magnetic Janus particles with anisotropy in the positioning of their magnetic dipole have been synthesized.<sup>7–14</sup> Importantly, while homogeneous

Received: January 16, 2019 Revised: May 13, 2019 Published: May 22, 2019

Department of Chemical Engineering, City College of the City University of New York (CUNY), New York, New York 10031, United States

<sup>&</sup>lt;sup>‡</sup>Department of Chemical Engineering, University of Puerto Rico—Mayagüez (UPRM), Mayaguez, Puerto Rico 00681, United States

magnetic particles have their magnetic dipole generally located at their center of mass, the dipole of a magnetic Janus particle is shifted away from its center of mass. The shift is either perpendicular to the direction of the dipole or parallel to the direction of the dipole. The unusual assembly behavior observed for particle systems with shifted dipoles has garnered the interest of many theoretical groups to develop models that describe colloids with the dipole shifted parallel, perpendicular, are or at varying angle with or without an external field. Our work studies the first case, i.e., the parallel-shifted dipole, more specifically, the iron oxide-capped magnetic Janus particle (Fe<sub>x</sub>O<sub>y</sub> JP) system.

The shifted dipole positioning in the  $Fe_xO_y$  JP system gives rise to unique interactions between the particles and variation in aggregate shape. For example, the staggered chains formed from  $Fe_{1-x}O$ -capped magnetic Janus particles ( $Fe_{1-x}O$  JPs) are shorter and wider than analogous linear chains formed by particles with dipoles of identical magnitude that are not shifted. The difference in geometry yields a difference in diffusivity, one of the two main driving forces of aggregation. The other driving force, chain dipole strength, is also influenced by the variance in geometry. An understanding of the structures that shifted dipole particles assemble into when exposed to a magnetic field can be used to predict the rate of assembly for a system of quasi-two-dimensional (2D) magnetic Janus particles. Figure 1 shows the various parameters relevant in aggregation and the geometry of the assembled structure.

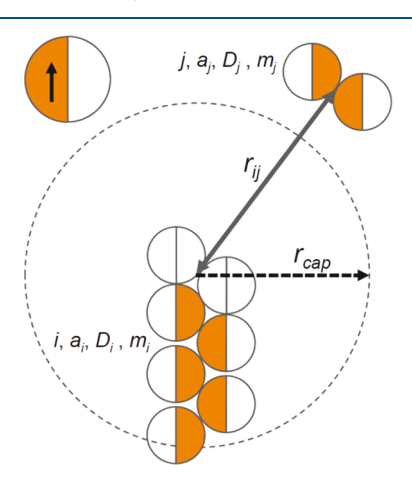


**Figure 1.** Schematic of a single Janus particle with shifted dipole indicated (upper left) and chain aggregation event. A pentuplet (bottom) aggregates with a doublet (upper right) as it traverses the distance between them  $(r_{ij})$ . When the aggregates are within the capture distance,  $r_{\rm cap}$  (dotted line), the pair will aggregate irreversibly. The driving forces of aggregation are the diffusive  $(D_i, D_j)$  and the magnetic properties  $(m_i, m_j)$  of each aggregate defined by the aggregate size  $(a_i, a_j)$ . The diffusive and magnetic properties for particles of a given type are a function of the number of particles in each aggregate (i, j).

Here, we introduce a theoretical model to describe the behavior observed for micron-sized magnetic Janus particles with shifted dipoles, using the example of  $Fe_{1-x}O$  Janus particles. Particles are experimentally monitored with an optical microscope and characterized with particle tracking software yielding aggregation information. The model proposed is used to predict the chain assembly rate of  $Fe_{1-x}O$  JP chains rather than merely finding a best-fit for the data after running the experiments. The efficacy of three

models is compared: a model driven entirely by diffusion, a model driven entirely by magnetic forces, and a hybrid of the two models that introduces a new parameter, the capture distance  $r_{\rm cap}$ . We arrive at a general model that enables the prediction of the  ${\rm Fe}_{1-x}{\rm O}$  JP chain assembly kinetics and propose that the model can be generalized for other assembling systems.

# **EXPERIMENTAL DETAILS**

Iron oxide-coated, sulfated-polystyrene Janus particles are synthesized by the monolayer and physical vapor deposition techniques developed and reported on previously.<sup>8</sup> Relevant information is summarized briefly.

**Monolayer Synthesis.** Microscope slides (1'  $\times$  3', Fisher Scientific) are cleaned in a Nochromix/sulfuric acid solution. The solution is prepared by mixing 4 g of Nochromix with 100 mL of deionized (DI) water for 20 min. Glass slides are placed in a container that allows the solution to fully coat them. The solution is added, and the slides are cleaned for 20 min. The slides are then removed and rinsed thoroughly with DI water. A slide—slide wedge is constructed from two slides with the two slides at a 30° angle with respect to each other. Of a 2.4  $\mu$ m sulfated-polystyrene particle solution (0.1% v/v, Invitrogen), 20  $\mu$ L is pipetted into the wedge. A motorized syringe pump is used to drag the top slide along the bottom one at a velocity of 200  $\mu$ m/s. As the slide moves at a constant rate, the particles form a monolayer on the bottom slide.

**Physical Vapor Deposition.** The particle monolayers are placed into a benchtop physical vapor deposition (PVD) machine (TedPella), as schematically shown in Figure 2A. A tungsten filament

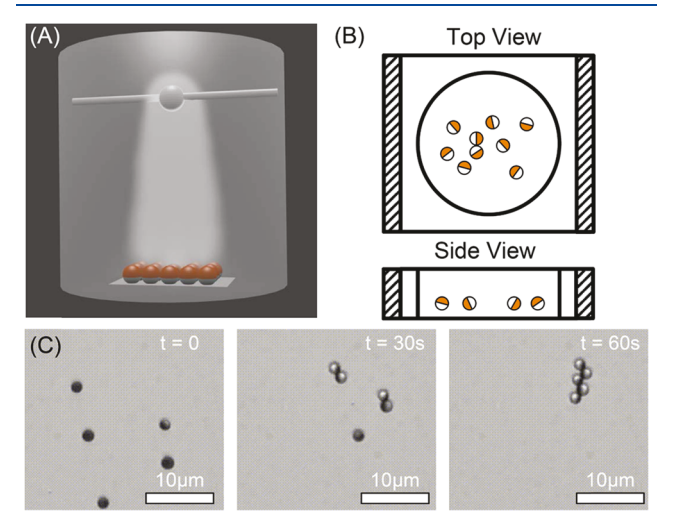


**Figure 2.** Fabrication and assembly setup for magnetic Janus particles. (A) Schematic of a physical vapor deposition onto a polystyrene particle monolayer. (B) Schematic of a 20  $\mu$ L particle suspension droplet after sandwiching between glass slides with double-sided sticky tape spacers (shaded areas). (C) Example of 2.4  $\mu$ m Fe<sub>1-x</sub>O Janus particles aggregating to form a chain with  $m_i = 5$  in an external magnetic field (0.08 T) applied parallel to the imaging plane.

in the PVD machine is loaded with iron pellets (Kurt J. Lesker Company). The pressure in the machine is lowered to 0.1 mPa. After the first pump-down cycle, a 3:1 argon/oxygen mixture is leaked into the chamber and the pressure is lowered again to purge any remaining ambient gas. The Ar: $O_2$  mixture is supplied at a constant 500 mPa, which provides the oxygen needed to oxidize the iron as it deposits on the particles.

For iron deposition, the filament is heated to the appropriate temperature needed for the desired deposition rate to produce  $Fe_{1-x}O$  (1.0  $\pm$  0.2 nm/s), and the shutter is opened.  $^8$  A thickness monitor records the amount of material deposited and dictates when to end

the deposition (typically 50 nm). When the deposition is finished, the machine is turned off, allowed to cool, and filled with  $N_2$  gas, and the  $Fe_{1-r}O$ -capped Janus particle monolayers are removed.

**Particle Assembly Tracking.** The monolayers of Janus particles are sonicated in DI water, and the solution is sonicated for 1 min before each trial in a sonication bath. Immediately after sonication, 14  $\mu$ L of ~0.1% (v/v) particle suspension is pipetted onto a slide with two pieces of double-sided sticky tape (Scotch double-sided tape, 160  $\mu$ m thickness) on two of its edges. Another slide is carefully placed on top of the first one while taking care to not allow capillary forces to displace the droplet of the solution. Sandwiching the water droplet between two spaced slides creates a flat, nearly cylindrical environment (~10 mm in diameter) for the particles to move around in (Figure 2B). The slide is then placed under a BX51 microscope from Olympus with a 5× objective.

The particles settle toward the bottom of the cell and hover slightly above the glass—water interface (Figure 2B). A system setup to observe settled particles limits their motion to two dimensions and allows the trajectories of the particles to be tracked in 2D. The height of the particles above the bottom cell wall is determined by the height at which the gravity is equal to the silica—polystyrene electrostatic repulsion force. Polystyrene particles ( $a = 1.2 \ \mu m$ ) are used because their equilibrium height is high enough to not dramatically impact their diffusion coefficient (i.e., diffusion coefficient is measured to be  $D_{PS} = 0.19 \pm 0.01$ , which is ~90% of the Stokes—Einstein prediction corresponding to particles located at >6 particle radii distance from the surface; see Granick et al.<sup>30</sup>).

In-house software is used to determine the initial concentration of particles by electronically counting the particles in a microscope image obtained from the assembled cell and subsequently dividing the area occupied by particles by the total frame area to determine the area fraction for the image. If the concentration is not close to the desired  $\sim\!\!1\%$  area fraction, the bulk solution is diluted by adding DI water or concentrated by removing the supernatant, a new cell is created, and the area fraction is checked again until solutions are obtained that yield a 1.0  $\pm$  0.1% area fraction.

A horseshoe magnet (0.08 T) is placed around the cell with its magnetic field aligned parallel to the imaging plane, and a video of the aggregation process is recorded after a 5 s delay. The particles maintain a constant dipole under these conditions and align the long axis of their caps with the external field. Four videos are captured at 5× magnification with an average of 1650  $\pm$  142 particles per video for 700 s at 3 fps. The particle size and area fractions are chosen to optimize the number of particles in the frame and the number of collisions that take place during an experiment run. Concentration profiles from these videos are averaged together with one standard deviation reported as the error. The video length is chosen to be 2 orders of magnitude larger than the Brownian time. Figure 2C shows the zoomed-in snapshots of an assembly of a quintet for illustrative purposes of an assembly event. Note, our initial field of view contains singlets (51  $\pm$  8%), doublets (27  $\pm$  4%), triplets (12  $\pm$  1%), and longer chains (11  $\pm$  5%) owing to the 5 s delay between adding the magnetic field and starting the video recording (see Figure S1 in the Supporting Information). Particle tracking software developed inhouse is used to process the four videos and obtain both contour data and particle trajectories (see Figure S2 and Video S1 in the Supporting Information). From the video analysis, relevant information is extracted such as the number of each aggregate type as a function of time (t), the rate of various chain length aggregation events  $(K_{ii})$ , diffusion coefficients  $(D_i)$ , the magnetic dipole strength  $(m_i, m_i)$ , the angle between the particles in the chains  $(\theta)$ , and the length of the chains  $(L_i)$ .

# RESULTS AND DISCUSSION

The data reported here is derived from the trajectory information collected from optical microscope videos. Videos are collected and processed with in-house particle tracking software. Subsequently, the trajectory information is used to determine the time evolution of the particle aggregate types

(theoretically described by a population balance equation known as the Smoluchowski coagulation equation) and the pair—pair distances of particle aggregates as they aggregate to form chains.

The length of the particle aggregates is measured, and the number of particles in each aggregate is counted for each frame of the experiment. The aggregation rate of chain length i is described generally by the Smoluchowski coagulation equation, eq. 1

$$\frac{\mathrm{d}n_i}{\mathrm{d}t} = n_i' = \frac{1}{2} \sum_{j=1}^{i-1} K_{i-j,j} n_{i-j} n_j - \sum_{j=1}^{\infty} K_{ij} n_i n_j \tag{1}$$

where  $K_{ij}$  and  $K_{i-j}$  are the rate constants (or "aggregation kernels") for the aggregation rates of each type of aggregation, and  $n_{ij}$   $n_{jj}$  and  $n_{i-j}$  are the concentrations of the chains of lengths i and j. The magnitude of the rate constants is determined by the forces driving aggregation. A general method that produces these rate constants would yield a complete description of the chain aggregation rate, as discussed below.

To empirically study the rate constants in an aggregating experimental system, the terms of the Smolukowski equation must be truncated to avoid dealing with an infinitely large system of coupled differential equations. The terms that can be neglected are determined by tracking a count of all events of each type occurring for each frame of the experiment. In the case studied here, 70% of aggregation events are found to involve at least one singlet (see Figure S3). Additionally, direct counting shows that for chains containing four or more particles ( $i \ge 4$ ) aggregating with a singlet, the ratio of collision rates to chain concentration ( $n_i$ ) is constant and equal to the product of the rate constant and the concentration of singlets ( $K_{1N}n_1$ )

$$\frac{\mathrm{rate}_{1,4}}{n_4} \approx \frac{\mathrm{rate}_{1,5}}{n_5} \approx ... \approx \frac{\mathrm{rate}_{1N}}{n_N} \approx K_{1N} n_1 \tag{2}$$

Therefore, only aggregation events  $K_{11}$ ,  $K_{12}$ ,  $K_{13}$ , and  $K_{1N}$  are included in the analysis. The  $K_{ij}$  values account for the most common aggregation events occurring in the  $\mathrm{Fe}_{1-x}\mathrm{O}$  JP system on the time scale of the experimental run (700 s) and introduce the additional term  $K_{1N}$  that combines all  $K_{1i}$  ( $i \geq 4$ ) to reduce the number of fitting variables. Any aggregation events not involving singlets are not included in the Smoluchowski fitting owing to their rare occurrence compared to singlet events. Then, a complete system of differential equations to solve as shown in eq 3a through eq 3e can be set up and implemented in a fitting algorithm to find  $K_{11}$ ,  $K_{12}$ ,  $K_{13}$ , and  $K_{1N}$ 

$$n_1' = -K_{11}n_1^2 - K_{12}n_1n_2 - \sum K_{1N}n_1n_j$$
 (3a)

$$n_2' = 0.5K_{11}n_1^2 - K_{12}n_1n_2 (3b)$$

$$n_3' = K_{12}n_1n_2 - K_{1N}n_1n_3 (3c)$$

$$n_4' = K_{1N} n_1 n_3 - K_{1N} n_1 n_4 \tag{3d}$$

For i > 4

$$n_i' = K_{1N}n_1n_{i-1} - K_{1N}n_1n_i = K_{1N}n_1(n_{i-1} - n_i)$$
(3e)

Applying the system of Smoluchowski coagulation equations, eqs 3a-3e, to the experimental data, numeric solutions to the differential equations are found with the four rate constants as

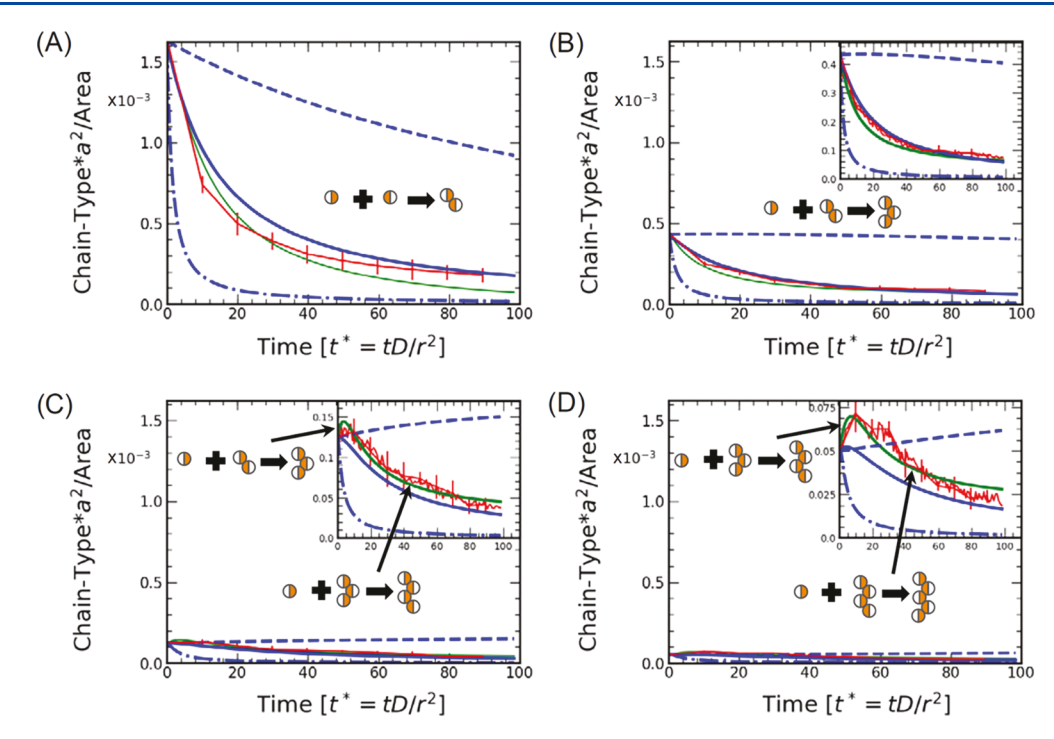


**Figure 3.** Area concentration of singlets (A), doublets (B), triplets (C), and quadruplets (D) nondimensionalized by the square of the particle radius *a* plotted vs dimensionless time. Red lines represent averaged experimental chain concentrations with one standard deviation, green lines are the Smoluchowski coagulation equation least-squares fits to the experimental data, dashed blue lines are the Brownian predictions, dash-dotted blue lines are the magnetic predictions, and solid blue lines are the capture distance predictions. The most prominent aggregation events are shown in each plot.

the degrees of freedom. From the initial solutions, the rate constants are adjusted, and the method is repeated iteratively until a least-squares fit of the experimental data is determined. The least-squares fit is performed on the four averaged data sets by minimizing the sum of the  $R^2$  values of each of the chain types, resulting in rate constants of  $K_{11} = 12$ ,  $K_{12} = 20$ ,  $K_{13} = 25$ , and  $K_{1N} = 30$ .

Area concentrations of various chain types are plotted in Figure 3. Note,  $a^2$  is chosen as a nondimensionalization factor to allow fitting with radius-independent models. Singlets, doublets, triplets, and quadruplets are plotted in Figure 3A–D, respectively. The Smoluchowski coagulation equation solution for each individual chain (green line) matches the averaged experimental data (red line) well, and the match is reflected in their high  $R^2$  values of 0.9. Over the plotted time period, the plotted chain concentrations are mostly being influenced by consumption events. The plots portray a high rate of consumption as all of the chain concentrations have a negative derivative for most of the experimental run.

Each chain has aggregation events most relevant to their concentration change, which are determined by comparison of the aggregation rates (experimentally determined to be  $K_{11}n_1n_1 > K_{12}n_1n_2 > K_{13}n_1n_3 > K_{1N}n_1n_i$  at short times) and direct counting of aggregation events. The relevant aggregation reactions are displayed on the plot of the respective concentration profile. For singlets, it is the singlet—singlet aggregation (as  $K_{11}n_1n_1 > K_{12}n_1n_2$ ). For doublets, it is the singlet—doublet aggregation (as  $0.5K_{11}n_1n_1 < K_{12}n_1n_2$ ), causing the concentration of doublets to only decrease owing to the initial presence of doublets in the solution. For triplets, a hint of triplet formation is observed at short times due to the singlet—double aggregation ( $K_{12}n_1n_3 > K_{13}n_1n_3$ ,  $n_3$  (t < 5) > 0), which is swiftly overcome by the singlet—triplet aggregation

 $(K_{12}n_1n_2 < K_{13}n_1n_3)$ , causing the concentration of triplets to decrease for most of the run. For quadruplets, the initial formation of quadruplets from the singlet—triplet aggregation is more apparent at short times  $(K_{13}n_1n_3 > K_{1N}n_1n_4, n_4'(t < 10) > 0)$  but is again overwhelmed by the singlet—quadruplet aggregation at  $t \approx 10$ , causing the concentration to decrease for the majority of the run. The maxima observed in Figure 3C,D are also confirmed by the chain counts shown in Figure S1.

**Model Development.** A comprehensive theory of particle chain aggregation would offer predictions of rate constants  $(K_{ij})$  for chain pairs of all lengths (i and j). The function for the rate constants will only require the driving forces for the aggregation of the individual aggregates, the chain lengths (i, j), the collision cross section, and the median interparticle distances  $(\langle r_{ij} \rangle)$ , which are a function of concentrations,  $n_i$ . The driving forces for aggregation are quantitatively the diffusive forces  $(D_i, D_j)$  and the magnetic forces  $(m_i, m_j)$ . The collision cross section is taken to be a function of only the single particle radius, a, and not of the chain lengths as the aggregations occur only tip-to-tip. Therefore, the function will be of the form depicted in eq. 4

$$K_{ij} = f(D_i, D_j, m_i, m_j, \mu, a, \langle r_{ij} \rangle)$$
(4)

The relative strength of the driving forces can be quantified by a Péclet number (Pe) defined as the ratio of the characteristic Brownian time,  $t_{\rm B} = 2a^2/(D_i + D_j)$ , to the characteristic magnetic time,  $t_{\rm M} = a/U$ , given by eq  $5^{31}$ 

$$Pe = \frac{t_{\rm B}}{t_{\rm M}} = \frac{r^{-4}\mu_0 m_i m_j}{\pi \mu D} \tag{5}$$

When Pe < 1, diffusive forces dominate; when Pe > 1, the magnetic forces dominate, and when Pe = 1, the two forces are

equivalent. The clearly defined boundary between the Brownian and the magnetic regimes (Pe = 1) allows for an unambiguous determination of the dominant force that drives assembly.

**Brownian Model.** In a system, in which diffusive forces are much stronger than magnetic forces ( $Pe \ll 1$ ), the "Brownian kernel" can be used to predict rate constants. Focusing on the Brownian kernel simplifies the function as Brownian forces neither are a function of the magnetic dipole strength of the chains nor are they dependent on the median interparticle distance (eq 6)

$$K_{ij}^{\text{Brown}} = f(D_i, D_j, a) \tag{6}$$

For individual components that aggregate when they enter  $r_i + r_j$  and are diffusing according to  $D_i$  and  $D_j$ , the general aggregation kernel,  $K_{ij}$  is shown in eq 7a. An explicit Brownian kernel,  $K_{ij}$  for 2D systems with the Stokes–Einstein diffusion and particle diameter collision distance is shown in eq 7b

$$K_{ij} = 2(D_i + D_j)(r_i + r_j)/(a_i + a_j)$$
(7a)

$$K_{ij}^{\text{Brown}} = 2(D_i + D_j) \tag{7b}$$

In dimensionless time, the rate constant is given in units of D. So, the rate constant for the singlet—singlet aggregation is  $K_{11}^*$  = 2. As the diffusion decreases with increasing length, <sup>4</sup> all other diffusion kernel rate constants are less than the singlet—singlet aggregation rate constant in the Brownian kernel model:  $K_{ij}^* \leq 2$ . Using the diffusion equations for spherocylinders described by Löwen, eq 8a, <sup>29</sup> we can express the diffusion coefficient for a general shifted dipole chain with eqs 8b–8d, where  $\theta$  is the angle a doublet makes with a line perpendicular to the magnetic field

$$D_{\text{chain}} = k_{\text{B}} T \left[ \frac{0.199 \ln \left(\frac{L}{\sigma}\right)}{L} + \frac{0.0169}{L} + \frac{0.0853 \sigma}{L^2} - \frac{0.00131 \sigma^2}{L^3} \right] \mu^{-1}$$
(8a)

$$D_1 = \frac{k_{\rm B}T}{3\pi\mu d} \tag{8b}$$

$$D_2 = \frac{0.0986 \ k_{\rm B}T}{\mu d} \tag{8c}$$

$$\begin{split} D_{i>2} &= k_{\rm B} T \Bigg[ \frac{0.199 \ln \left( \frac{\cos(\theta)d(i-1)+d}{\sin(\theta)d+d} \right)}{\cos(\theta)d(i-1)+d} \\ &+ \frac{0.0169}{\cos(\theta)d(i-1)+d} + \frac{0.0853 \left( \sin(\theta)d+d \right)}{\left( \cos(\theta)d(i-1)+d \right)^2} \\ &- \frac{0.00131 \left( \sin(\theta)d+d \right)^2}{\left( \cos(\theta)d(i-1)+d \right)^3} \Bigg|_{\mu^{-1}} \end{split} \tag{8d}$$

In eq 8a,  $\sigma$  is the width of the cylinder and L is the length of the cylinder.  $D_1$  is the diffusion coefficient of a sphere and

approximates a singlet, eq 8b. D2 is the diffusion coefficient for a spherocylinder with a length of two particle diameters, L =2d, and a width of 1 diameter,  $\sigma = d$ , and approximates a doublet, eq 8c.  $D_{i>2}$  is the diffusion coefficient of a longer spherocylinder and approximates longer chains. The  $\sigma$  and L of longer chains (n > 2) are affected by the angle  $\theta$  between particles in the chain, where i represents the number of particles in a chain. As  $\theta$  is often the reported characteristic of shifted dipole particles, eq 8a is modified to characterize the geometry of chains with an axial shift, as shown in eq 8d.  $\theta$  is determined by the shift in the dipole and determines the geometric variation from dipoles that are located at the center of mass. For triplets and longer chains, a rectangle of minimum size encapsulating the aggregate is defined through contour detection, and their diffusion coefficients are calculated by taking the long side as the length  $(\cos(\theta)d(i-1)+d)$  and the short side as the width  $(\sin(\theta)d + d)$ , as shown in eq 8d. The dimensions of the rectangle reflect the relationship between the dipole shift and geometry of the aggregate. Diffusion directly impacts the Smoluchowski coagulation equation constants in the diffusion model from eqs 7a and 7b.

**Magnetic Model.** The other extreme regime is when magnetic forces are much greater than diffusive forces ( $Pe \gg 1$ ). Here, aggregation occurs due to the dipole–dipole attraction of the chains at their tips (eq 9)

$$K_{ij}^{\text{magnetic}} = f(m_i, m_j, \mu, a, \langle r_{ij} \rangle)$$
(9)

The dipole force between a chain with its closest neighbor (excluding other chains in the system) is given by the dipole—dipole interaction force between the two chains, eq 10, where the bold symbols are vector properties

$$F(r, m_1, m_2) = \frac{-3\mu_0}{4\pi r^5} \left[ (\mathbf{m_1 \cdot r}) \mathbf{m_2} + (\mathbf{m_2 \cdot r}) \mathbf{m_1} + (\mathbf{m_1 \cdot m_2}) \mathbf{r} - \frac{5(\mathbf{m_1 \cdot r})(\mathbf{m_2 \cdot r})}{r^2} \mathbf{r} \right]$$
(10)

In radial units for aligned particles, eq 10 simplifies to eq 11

$$F_{\rm m}(r, m_1, m_2) = \frac{-3\mu_0 m_1 m_2}{2\pi r^4} \tag{11}$$

For systems in the Stokes flow regime, forces are equal to the viscous drag force. The drag force for a single sphere is defined by eq 12

$$F_{\rm D} = 6\pi\mu av \tag{12}$$

Using the constraint that the drag force opposes the magnetic attraction,  $F_{\rm m}=-F_{\rm D}$ , we obtain an expression for the velocity (eq 13), which yields a solvable differential equation for r as a function of time

$$r' = \nu = r^{-4} \frac{\mu_0 m_1 m_2}{4\pi^2 \mu a} \tag{13}$$

Solving eq 13 yields a pair trajectory, eq 14, with the constant *C* defined in eq 15

$$r(t) = \sqrt[5]{r_0^5 - Ct} \tag{14}$$

$$C = \frac{5\mu_0 m_1 m_2}{4\pi^2 \mu a} = \frac{5r^4 PeD}{a} \tag{15}$$

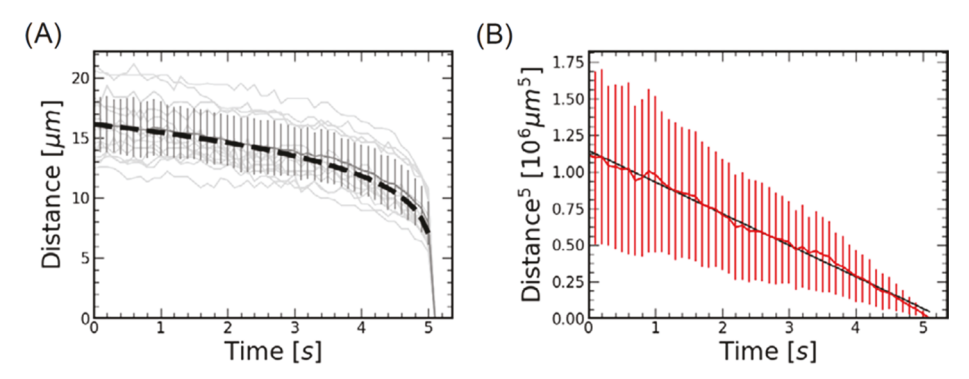


**Figure 4.** Determination of the magnetic moment and constant C, eq 15. (A) Plot of the distance between all aggregating singlet pairs vs time. With a relative time of  $t_r = 5$  used as the instant of completed aggregation for the particle pairs. The light gray lines are individual pair aggregation events. The dark gray line is an average of all pairs observed, and the bars represent one standard deviation. The black dashed line is the best-fit for the averaged data. Times before  $t_r = 0$  do not show a monotonically decreasing trend and are not pictured as they are in the stochastic Brownian regime. (B) Average particle pair data is plotted as the distance raised to the fifth power vs time. The experimental data is shown in red with bars indicating one standard deviation. The black line shows a linear least-squares fit  $(r^5 = -10^{5.33} t + 10^6, R^2 = 0.99)$ .

Equation 14 dictates the time it takes long chains of a given type to aggregate from a given distance when magnetic forces dominate ( $Pe \gg 1$ ). Here,  $r_0$  is the initial distance.

The magnetic dipole strength,  $m_1$ , needed for the calculation of constant C is a function of cap preparation<sup>8</sup> and determines the attractive force between two particles during the aggregation process. Magnetic dipole moments of Janus particles can be determined in various ways using the magnetic rolling,<sup>32</sup> particle—particle pair interaction plots,<sup>33</sup> or traditional SQUID-based MPMS measurements.<sup>33</sup> Here, the dipole strength is determined by plotting particle distances as a function of time for all aligned singlet pairs, and each is fitted to the pair trajectory equation, eq 14.

An assumption of aligned, deterministic dipole-dipole interaction is used for determining the strength of the dipole,  $m_1$ . The model assumes an  $r^5 \propto t$  dependence, eq 14, where r is the distance between two aggregating pairs and t is the time. The time dependence can be verified experimentally by plotting the distance, r, between each aggregating pair as a function of time (Figure 4A), where  $t_r = 0$  is iteratively determined by finding the time where r changes from a purely stochastic function to a monotonically decreasing function. Next, all particle pair functions obtained are normalized by the point of completed aggregation,  $t_r = 5$ , and plotted. Averaging of all aggregating pairs (dashed line in Figure 4A) leads to an r vs t curve, where  $r = 16.20 \ \mu \text{m}$  at  $t_r = 0$ . Plotting of the average as an  $r^5$  over t plot is then fitted with a linear least-square bestfit with a C constant of  $C = -10^{5.33}$  and an  $R^2$  value of 0.99, confirming the  $r^5 \propto t$  dependence (Figure 4B, black line). Using the analysis, the average of the dipole strength is determined to be  $\sim 0.05$  A  $\mu m^2$  for the Fe<sub>1-x</sub>O JP system studied here, which is consistent with earlier predictions on the dipole strength per volume of  $Fe_{1-x}O$  reported by Ren et al. of 132 emu/cm<sup>3.8</sup> The pair trajectory equation, eq 14, is converted into a Smoluchowski coagulation equation kernel by determining the median interparticle distance for the chains. The median interparticle distance is given by considering a random distribution of two-dimensional particles and finding the median distance of such a distribution,<sup>34</sup> eq 16

$$r_{ij} = \sqrt{\frac{\ln(2)}{\pi n_{ij}}} \tag{16}$$

Using the distance,  $r_{ij}$ , in the pair trajectory equation, an expression for the half-life can be obtained (eq 17), as half of the chains are within the median interparticle distance and half of the chain pairs will have aggregated after they deterministically aggregate according to the pair trajectory equation (eq 14)

$$t_{1/2} = \frac{r_{ij}^{5}}{C} \tag{17}$$

The half-life equation for second-order reactions (eq 17) provides an expression for the magnetic kernel (eq 18)

$$K_{ij}^{\text{magnetic}} = \frac{C}{n_{ij}r_{ij}^{S}} = \frac{Sr^{4}PeD}{an_{ij}r_{ij}^{S}}$$
(18)

Using the known system constants (concentration, dipole strength, diffusion coefficient, and particle size), the experimentally determined kernels can be compared to the theoretically predicted kernels. The measured magnetic dipole for a singlet is compared to a rotation averaged dipole with a bias toward alignment with the external magnetic field using a probability density function shown in eq 19, making the net force with its nearest-neighbor less than that of an aligned dipole

PDF(
$$i = 1, 0 < \theta < 2\pi$$
)  $\sim e^{F_{\text{aligned }} \cos(\theta)/kT}$  (19)

The net force,  $F_{\rm net}$  of the other chains with their neighbors is larger than that of singlets, as they have more particles. More specifically, for aligned interactions ( $\theta=\pi/2$ ),  $F_{\rm net-aligned}$  linearly increases as per eq 20 (where i is the number of particles in the aggregate) and they are stabilized in an aligned orientation due to additional particles in the chain

$$F_{\text{net-aligned}}(i) = iF_{\text{net-aligned}}$$
 (20)

Using the measured magnetic dipole and concentrations of the particle aggregates, the values for the rate constants are calculated as  $K_{11} = 150$ ,  $K_{12} = 180$ ,  $K_{13} = 206$ , and  $K_{14} = 226$ .

**Capture Distance Model.** If the time it takes a pair to assemble from the Pe=1 distance is significantly less than the time it takes the particles to enter within this distance, then the Pe=1 distance can be defined as a capture distance,  $r_{\rm cap}$ , as shown in Figure 1. A capture distance model requires

information about the viscosity, diffusion coefficients, dipole strengths, and the particle radius of the components eq 21

$$K_{ij}^{\text{cap}} = f(\mu, D_i, D_j, m_i, m_j, a)$$
 (21)

When a pair of particles enter within  $r_{\rm cap}$ , the particles will deterministically aggregate on a short time scale. The fast, deterministic behavior of particles within  $r_{\rm cap}$  allows the use of eq 7a by substituting the particle radius in eq 8a for  $r_{\rm cap}$  defined in eqs 22a and 22b (by solving eq 5 for Pe=1)

$$r_{\rm cap} = \sqrt[4]{\frac{{\mu_0 m_1}^2}{\pi \mu D}} \tag{22a}$$

$$r_{ij-cap} = \sqrt[4]{\frac{2\mu_0 m_1^2 ij}{\pi \mu (D_i + D_j)}}$$
 (22b)

Solving eqs 22a and 22b for our system, we find a capture distance of  $r_{\rm cap} = 16~\mu{\rm m}$  for the singlet—singlet interactions, which is in remarkable good agreement with the distance  $r = 16~\mu{\rm m}$  at  $t_r = 0$  obtained for the average shown in Figure 4A. Substituting the capture distance into eq 7a, we find a prediction for the  $K_{11}$  to be 12.5. As the attractive dipole force increases linearly with increasing chain length and the diffusion coefficient decreases according to eqs 8a–8d, the general expression for rate constants in the capture distance model is given by eq 23, where  $a_i$  and  $a_j$  refer to the radii of the interacting aggregates (Figure 1)

$$K_{ij}^{\text{cap}} = 2(D_{i-\text{chain}} + D_{j-\text{chain}}) \frac{r_{ij-\text{cap}}}{a_i + a_j}$$
(23)

Figure 4A already independently confirms the validity of our capture distance estimates in two ways: (1) the particle pairs act stochastically as Brownian particles at distances greater than the capture distance,  $r_{\rm cap}=16~\mu{\rm m}$ , and (2) the dipole calculated by the average best-fit for the pairs produces a dipole that corresponds to the proposed capture distance. In addition, the analysis of the cumulative probability function of nearest-neighbors for all chains was performed (see Figure S4 in the Supporting Information). The analysis shows that the median nearest-neighbor distance obtained from our 2.4  $\mu{\rm m}$  Fe<sub>1-x</sub>O JP particle system is best fitted with a hard sphere system of particles with  $d=15~\mu{\rm m}$ , further supporting our capture distance model with  $r_{\rm cap}=16~\mu{\rm m}$ .

Equation 23 can be used in combination with eqs 8a-8d, 22a, and 22b as a full characterization of the general rate constants with the inputs of a finite list of attributes of an individual particle and the solution the particles are in: temperature, viscosity, dipole moment, and dipole shift.

**Hydrodynamic Forces.** Particle—particle hydrodynamic forces also influence the aggregation rate of aggregating systems. The particle—particle approach slows down due to fluid flow fields generated by the two particles as they move. At short distances, hydrodynamic forces compete with Brownian and magnetic forces. These forces can be accounted for by modifying each model to account for the slowing, hydrodynamic force. The Brownian model can be modified by lowering the effective diffusion coefficient of the chains according to hydrodynamic approximations of diffusion coefficients of approaching pairs.<sup>35</sup> Accounting for the hydrodynamic forces (eq 24a)<sup>36</sup> lowers the rate constant of the diffusion model. Magnetic models can likewise lower their

approach velocity, incorporating hydrodynamic resistance between pairs

$$F_{\rm L,\infty} = \frac{3}{2}\pi\mu a^2 v/r \tag{24a}$$

$$F_{\rm L,\infty}/F_{\rm M} = \frac{\frac{3}{2}\pi\mu a^2 v}{r} / \frac{-3\mu_0 m_1 m_2}{2\pi r^4}$$
 (24b)

However, for many systems, magnetic forces will be much greater than hydrodynamic forces. To determine if we are in a regime where the magnetic forces are much greater than the hydrodynamic forces during aggregation-rate-relevant steps in the process, we take a ratio of the hydrodynamic forces to the magnetic forces (eq 24b) at our capture distance. If  $F_{\rm L,\infty}/F_{\rm M} \ll 1$ , then the magnetic forces dominate and the hydrodynamic forces can be ignored. In our system,  $F_{\rm L,\infty}/F_{\rm M} \sim 10^{-5}$ . Therefore, the hydrodynamic forces do not need to be taken into account when approximating rate constants.

The Péclet number of a system of magnetic particles determines the aggregation regime the particles are in. When  $Pe \ll 1$ , the diffusive model has been shown to accurately predict aggregation constants, eq 7b. When  $Pe \gg 1$ , the magnetic model accurately predicts the aggregation rate constants, eq 18. When Pe is of intermediate value, the capture distance model accurately predicts the aggregation rate constants, eq 23.

Using these models as a foundation, the equations for nonshifted magnetic particle aggregation rates can be modified to determine the aggregation rates of particles with an arbitrary shift. Accounting for the shift's effect on the aggregation rate is done by modeling the diffusion of particle aggregates as spherocylinders and applying the correct diffusion coefficients for the aggregates.

Each model offers clear predictions for the Smoluchowski coagulation equation rate constants. These rate constants can be compared against the best-fit rates to see which model best represents the  $\mathrm{Fe}_{1-x}\mathrm{O}$  JP system. Table 1 summarizes the direct rate measurements based on the counting of each aggregation event, the various rate constants for each model, and the  $R^2$  value averages of best-fits.

Table 1. Aggregation Rate Constants from Various Models

	constant				
model	$K_{11}^{a}$	$K_{12}^{a}$	$K_{13}^{a}$	$K_{14}^{a}$	average R <sup>2</sup> b
direct count	12	60	58	57	$0.89 \pm 0.04$
equation fit eq 1	12	20	25	30 <sup>c</sup>	$0.94 \pm 0.02$
Brownian eq 7b	2	2	2	1	$-9 \pm 2$
magnetic eq 18	150	180	206	226	$-0.24 \pm 1.00$
capture dis eq 23	15	18	21	23	$0.92 \pm 0.02$

<sup>a</sup>Rate constant obtained from averaged data of four videos with 1650  $\pm$  142 particles. <sup>b</sup>Average  $R^2$  value from best-fit of  $K_{11}$ ,  $K_{12}$ ,  $K_{13}$ , and  $K_{14}$ . <sup>c</sup> $K_{14} = K_{1N}$ , see Experimental Details for Smoluchowski coagulation equation rate constants.

The "direct count" row is information-collected by tracking each particle and counting the number of aggregation events happening in a given moment. As the system is optically observed, each individual chain formation event can be counted, resulting in a count of chains for each instance of the experiment. The instantaneous rates are averaged over a small time interval to eliminate moments in which no

aggregation occurs. The counts are then normalized over the time interval to obtain a rate for the given event type. The direct count rate is then divided by the appropriate concentrations to obtain the rate constant for the event. The direct count of the rate constant measurement is the most accurate method of direct rate measurement, and the accuracy is reflected in the  $R^2$  value. The divergence of the direct count measurement from the data comes from the variability of the rate constant over multiple intervals. The direct count gives a reasonable approximation for the average  $R^2$  values to be expected in sufficiently explanatory models ( $R^2 \sim 0.9$ ).

The "equation fit" row is a least-squares minimization of the Smoluchowski coagulation equation (eq 1) to the data. The rate constants are adjusted until the average  $R^2$  is minimized. The equation fit provides an upper bound for how close to 1 the  $R^2$  value can be. The divergence of the equation fit from a perfect fit comes from the variability between experimental initial states, the inherent stochasticity of the experiments, the fact that experiments are discrete counts rather than concentrations in the infinitely large sample size limit, and any additional physics (e.g., the impact of nonuniform drift) not accounted for. The equation fit demonstrates that the Smoluchowski coagulation equation is a valid model of the data, as  $R^2$  is found to be  $0.94 \pm 0.02$ .

The "Brownian" row shows the accuracy of the Brownian model with cylindrical approximations for the aggregate diffusion coefficients (eq 7b). Unsurprisingly, we see that all rate constants are much lower than the direct count data or equation fit data and the  $R^2$  value is negative meaning that the Brownian kernel is not a good model for the system. The poor fit shows that assuming an aggregation driven purely by the Brownian motion is insufficient to model the Fe<sub>1-x</sub>O JP system and tells us that modeling the system as "Brownian particles that irreversibly aggregate when they collide" is incomplete and additional driving forces need to be accounted for.

The "magnetic" row shows the accuracy of the magnetic model with aligned dipoles (eq 18). It can be seen that the magnetic model rate constants are much higher than the rate constants in the direct count data or equation fit data, and the  $R^2$  value is, again, negative indicating a bad fit and an incomplete model. The poor fit being far below the actual concentration profile data shows that the deterministic, aligned magnetic model overrepresents the dipole moment as a driving force in aggregation. The particles are not perfectly in line with their nearest-neighbor and such a model would be more suited for symmetric forces.

The "capture dis" row shows the accuracy of the capture distance model (eq 23). In the capture distance model, it can be seen that the rate constants are similar to the rate constants in the first two rows and increase as longer chains are involved. The average  $R^2$  value is close to 0.9, indicating that the capture distance model is a good fit for the system. The accuracy of the fit is reflected in how close the concentration profiles for the data, fit, and capture distance model are with each other (Figure 3), i.e., accounting for Brownian forces and angle-dependent magnetic forces is sufficient to model aggregation rates for the  $Fe_{1-x}O$  JP system.

The capture distance model can be used as a basis to predict the concentration profiles over time for all systems of shifted dipole magnetic particles. When the median interparticle distance is large enough to make hydrodynamic forces negligible in their contribution to the aggregation rate and any additional forces are negligible, the capture distance model can be used directly to accurately determine the concentration profiles of the system. With the concentration profiles known, a connection needs to be made between an aggregate distribution and the viscosity of the system to predict a rheological response in the quasi-2D  $\operatorname{Fe}_{1-x}O$  JP system. The capture distance model as formulated in eq 23 allows the variation of particle diameter, viscosity, and temperature through the diffusion coefficient and the magnitude of attractive interaction (see eq 23), thereby reducing the need for lengthy synthetic trials to explore an arbitrary amount of systems quickly.

The ratio of the actual to initial chains  $(n_c/n_0 = (\sum n_i)/n_0$  with i = 1-10) is plotted in Figure 5 for experimental data (red

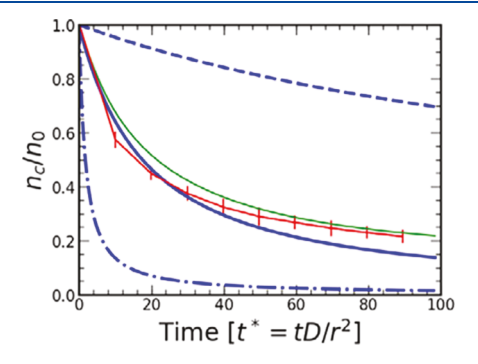


**Figure 5.** Ratio of the actual to initial chains  $(n_c/n_0)$  vs time in dimensionless units. Red line represents averaged experimental chain fraction with one standard deviation, green line is the Smoluchowski coagulation equation least-squares fit to the experimental data, dashed blue line is the Brownian prediction, dashed-dotted blue line is the magnetic prediction, and solid blue line is the capture distance prediction for the total number of chains.

line with error bars) and the four models (green line, the Smoluchowski coagulation equation least-squares fit, dashed blue line, the ratio predicted by the Brownian model, dashdotted line, the ratio predicted by the magnetic model, and solid blue line, the ratio predicted by the capture distance model). Summing the individual Smoluchowski concentration profiles shown in Figure 3 and including longer chains (up to i = 10) yield the sum of the individual Smoluchowski coagulation equation solutions  $(n_c^{\text{Smol}})$ .  $n_c^{\text{Smol}}/n_0$  (green line) is found to have good agreement with the experimental data with an  $R^2 = 0.91$  comparable to the  $R^2$  values obtained from the Smoluchowski fit for the individual chain types, Figure 3 (green lines) and Table 1. Similarly, the experimentally found  $n_c/n_0$  ratio agrees well with the ratio predicted by the capture distance model ( $R^2 = 0.89$ ), while the Brownian and magnetic models again fail to predict the correct ratio. The ability to fit the experimental data for the individual chain formation and the overall number of aggregates,  $n_c$ , independently demonstrate the validity of the fundamental description of the system, i.e., a balance of formation and aggregation events for the individual aggregate types that naturally tends toward longer and fewer chains at long times.

The capture distance model has limitations. It does not currently account for hydrodynamic forces. Fortunately, hydrodynamic forces are unimportant for systems when the magnetic force is greater than the lubrication-squeezing force at the capture distance, as is the case for the  $Fe_{1-x}O$  JP system. But such forces could be added as a "diffusion-reducing" force, making the diffusion component of the rate constant equations

a function of the nearest-neighbor distance. Another limitation is the minimal discussion of shearing and breakup. Our system involved no shear forces or breakup, but shear forces and breakup will be common in many magnetorheological systems.<sup>2</sup> These influences on concentration profiles have been explored in the literature<sup>37</sup> but will need to be modified for shifted dipole systems by use of our capture distance model.

Through the development of the capture distance model, we have gained knowledge of the aggregation behavior of magnetic Janus particles with shifted dipoles. The quasi-2D model shows good agreement with experimentally observed chain formation in the 2.4  $\mu$ m Fe<sub>1-x</sub>O JP system and provides a better understanding of the relationship between the inherently shifted dipole of the Janus particle, the resulting structure of the aggregate, and the rate of aggregation. More specifically, the model shows that the impact of the shifted dipole can be included through careful consideration of the aggregate dimensions that, in turn, impact the diffusion coefficients of the aggregates during chain formation and aggregation rate. Connecting the aggregate structure and number to viscosity will require the study of the mechanical properties of the chains to predict a rheological response. In addition to shifted magnetic dipole systems, the capture distance model can also be applied to characterize the aggregation rates of systems with forces acting at a distance that are anisotropic. For instance, the electrical dipole forces that cause charged Janus particles to assemble.<sup>38</sup>

## SUMMARY AND CONCLUSIONS

The aggregation of staggered magnetic particle chains from  $\mathrm{Fe_{1-x}O}$  Janus particles has been studied, and the staggered geometry has been found to be a relevant difference between shifted magnetic dipole particles and particles with a magnetic dipole in their center. The change in geometry can be accounted for in the rate constants by modeling how the magnetic dipole shift of the individual particles changes the geometry of the chains, using a spherocylindrical geometry in a modified diffusion coefficient expression. The modified diffusion is an effect that can reduce diffusion (and therefore rate constants) by as much as 17%.

The capture distance model for the rate constants is then used to predict the concentration profiles of each cluster type and is found to accurately predict the time evolution of the concentration profiles. We recommend the capture distance model with modified diffusion constants for use in related systems to find the time evolution of their aggregate concentration profiles. The required variables of temperature, viscosity, dipole moment, and dipole shift can be input into the analytic expression of the capture distance model to find the net chain aggregation rate and each specific chain concentration profile. The ability to model individual chain concentration profiles for systems involving particles with shifted dipoles enables a better understanding and prediction of the rheological response of magnetic JP systems.

## ASSOCIATED CONTENT

# S Supporting Information

The Supporting Information is available free of charge on the ACS Publications website at DOI: 10.1021/acs.langmuir.9b00163.

Particle tracking analysis, collision event counting, chain concentrations, and capture distance/nearest-neighbor distributions (PDF)

Assembly of 2.4  $\mu$ m Fe<sub>1-x</sub>O JP system in an external magnetic field of 0.08 T applied parallel to the imaging plane (AVI)

### AUTHOR INFORMATION

#### **Corresponding Author**

\*E-mail: kretzschmar@ccny.cuny.edu.

#### ORCID 🏻

Ubaldo M. Córdova-Figueroa: 0000-0003-4891-5325

Ilona Kretzschmar: 0000-0001-7636-1679

#### Notes

The authors declare no competing financial interest.

### ACKNOWLEDGMENTS

This work was supported by the National Science Foundation under Award CBET-1705565. T.W.L. acknowledges a fellowship from Leonard Schuchman.

### REFERENCES

- (1) Furst, E. M.; Gast, A. P. Dynamics and lateral interactions of dipolar chains. *Phys. Rev. E* **2000**, *62*, 6916–6925.
- (2) Koo, J.-H.; Fernando, D. G.; Mehdi, A. A comprehensive analysis of the response time of MR dampers. *Smart Mater. Struct.* **2006**, *15*, 351.
- (3) Dreyfus, R.; Baudry, J.; Roper, M. L.; Fermigier, M.; Stone, H. A.; Bibette, J. Microscopic artificial swimmers. *Nature* **2005**, 437, 862–865.
- (4) Martínez-Pedrero, F.; Tirado-Miranda, M.; Schmitt, A.; Callejas-Fernández, J. Formation of magnetic filaments: A kinetic study. *Phys. Rev. E* **2007**, *76*, No. 011405.
- (5) Bharti, B.; Kogler, F.; Hall, C. K.; Klapp, S. H. L.; Velev, O. D. Multidirectional colloidal assembly in concurrent electric and magnetic fields. *Soft Matter* **2016**, *12*, 7747–7758.
- (6) Kogler, F.; Velev, O. D.; Hall, C. K.; Klapp, S. H. L. Generic model for tunable colloidal aggregation in multidirectional fields. *Soft Matter* **2015**, *11*, 7356–7366.
- (7) Ge, J.; Hu, Y.; Zhang, T.; Yin, Y. Superparamagnetic Composite Colloids with Anisotropic Structures. J. Am. Chem. Soc. 2007, 129, 8974–8975.
- (8) Ren, B.; Ruditskiy, A.; Song, J. H.; Kretzschmar, I. Assembly Behavior of Iron Oxide-Capped Janus Particles in a Magnetic Field. *Langmuir* **2012**, 28, 1149–1156.
- (9) Ruditskiy, A.; Ren, B.; Kretzschmar, I. Behaviour of Iron Oxide (Fe<sub>3</sub>O<sub>4</sub>) Janus Particles in Overlapping External AC Electric and Static Magnetic Fields. *Soft Matter* **2013**, *9*, 9174–9181.
- (10) Bharti, B.; Velev, O. D. Assembly of Reconfigurable Colloidal Structures by Multidirectional Field-Induced Interactions. *Langmuir* **2015**, *31*, 7897–7908.
- (11) Smoukov, S. K.; Gangwal, S.; Marquez, M.; Velev, O. D. Reconfigurable responsive structures assembled from magnetic Janus particles. *Soft Matter* **2009**, *5*, 1285–1292.
- (12) Steinbach, G.; Nissen, D.; Albrecht, M.; Novak, E. V.; Sánchez, P. A.; Kantorovich, S. S.; Gemming, S.; Erbe, A. Bistable self-assembly in homogeneous colloidal systems for flexible modular architectures. *Soft Matter* **2016**, *12*, 2737–2743.
- (13) Baraban, L.; Makarov, D.; Albrecht, M.; Rivier, N.; Leiderer, P.; Erbe, A. Frustration-induced magic number clusters of colloidal magnetic particles. *Phys. Rev. E* **2008**, *77*, No. 031407.
- (14) Sacanna, S.; Rossi, L.; Pine, D. J. Magnetic Click Colloidal Assembly. J. Am. Chem. Soc. 2012, 134, 6112-6115.
- (15) DeGennes, P. G. Soft Matter (Nobel Lecture). Angew. Chem., Int. Ed. 1992, 31, 842-845.

(16) Erhardt, R.; Zhang, M. F.; Boker, A.; Zettl, H.; Abetz, C.; Frederik, P.; Krausch, G.; Abetz, V.; Muller, A. H. E. Amphiphilic Janus micelles with polystyrene and poly(methacrylic acid) hemispheres. J. Am. Chem. Soc. 2003, 125, 3260–3267.

- (17) Zhang, Z. L.; Glotzer, S. C. Self-assembly of patchy particles. *Nano Lett.* **2004**, *4*, 1407–1413.
- (18) Hong, L.; Cacciuto, A.; Luijten, E.; Granick, S. Clusters of charged Janus spheres. *Nano Lett.* **2006**, *6*, 2510–2514.
- (19) Lattuada, M.; Hatton, T. A. Synthesis, properties and applications of Janus nanoparticles. *Nano Today* **2011**, *6*, 286–308.
- (20) Perro, A.; Reculusa, S.; Ravaine, S.; Bourgeat-Lami, E. B.; Duguet, E. Design and synthesis of Janus micro- and nanoparticles. *J. Mater. Chem.* **2005**, *15*, 3745–3760.
- (21) Hong, L.; Jiang, S.; Granick, S. Simple Method to Produce Janus Colloidal Particles in Large Quantity. *Langmuir* **2006**, 22, 9495–9499.
- (22) Novak, E. V.; Pyanzina, E. S.; Kantorovich, S. S. Behaviour of magnetic Janus-like colloids. *J. Phys.: Condens. Matter* **2015**, 27, No. 234102.
- (23) Kantorovich, S.; Weeber, R.; Cerdà, J. J.; Holm, C. Magnetic particles with shifted dipoles. *J. Magn. Magn. Mater.* **2011**, 323, 1269–1272.
- (24) Kantorovich, S.; Weeber, R.; Cerda, J. J.; Holm, C. Ferrofluids with shifted dipoles: ground state structures. *Soft Matter* **2011**, *7*, 5217–5227.
- (25) Weeber, R.; Klinkigt, M.; Kantorovich, S.; Holm, C. Microstructure and magnetic properties of magnetic fluids consisting of shifted dipole particles under the influence of an external magnetic field. *J. Chem. Phys.* **2013**, *139*, No. 214901.
- (26) Piastra, M.; Virga, E. G. Phase polarity in a ferrofluid monolayer of shifted-dipole spheres. *Soft Matter* **2012**, *8*, 10969–10981.
- (27) Abrikosov, A. I.; Sacanna, S.; Philipse, A. P.; Linse, P. Self-assembly of spherical colloidal particles with off-centered magnetic dipoles. *Soft Matter* **2013**, *9*, 8904–8913.
- (28) Gartland, E. C.; Virga, E. G. An analytic mean-field model for the magnetic response of a ferrofluid monolayer. *Soft Matter* **2013**, *9*, 5991–6008.
- (29) Löwen, H. Brownian dynamics of hard spherocylinders. *Phys. Rev. E* 1994, 50, 1232–1242.
- (30) Anthony, S. M.; Hong, L.; Kim, M.; Granick, S. Single-Particle Colloid Tracking in Four Dimensions. *Langmuir* **2006**, 22, 9812–
- (31) Darras, A.; Opsomer, E.; Vandewalle, N.; Lumay, G. Superparamagnetic colloids in viscous fluids. *Sci. Rep.* **2017**, *7*, No. 7778.
- (32) Fei, W.; Driscoll, M. M.; Chaikin, P. M.; Bishop, K. J. M. Magneto-capillary dynamics of amphiphilic Janus particles at curved liquid interfaces. *Soft Matter* **2018**, *14*, 4661–4665.
- (33) Ren, B. Magnetic Janus Particles and Their Applications. Doctoral Thesis, City College of New York, New York, 2014.
- (34) Tournus, F. Random nanoparticle deposition: inter-particle distances in 2D, 3D, and multilayer samples. *J. Nanopart. Res.* **2011**, 13, 5211.
- (35) Guazzeli, E.; Morris, J. F. A Physical Introduction to Suspension Dynamics; Cambridge University Press, 2012.
- (36) Zhang, W.; Noda, R.; Horio, M. Evaluation of lubrication force on colliding particles for DEM simulation of fluidized beds. *Powder Technol.* **2005**, *158*, 92–101.
- (37) Tolpekin, V. A.; Duits, M. H. G.; van den Ende, D.; Mellema, J. Aggregation and Breakup of Colloidal Particle Aggregates in Shear Flow, Studied with Video Microscopy. *Langmuir* **2004**, *20*, 2614–2627.
- (38) Zhang, L.; Zhu, Y. Directed Assembly of Janus Particles under High Frequency ac-Electric Fields: Effects of Medium Conductivity and Colloidal Surface Chemistry. *Langmuir* **2012**, *28*, 13201–13207.